TWO MEDICAL IMAGING PROCESSING TECHNIQUES FOR USE IN ACOUSTIC

NEUROMA REMOVAL AND COCHLEAR PROSTHETIC IMPLANTATION

By

Kepra L McBrayer

Thesis

Submitted to the Faculty of the

Graduate School of Vanderbilt University

in partial fulfillment of the requirements

for the degree of

MASTER OF SCIENCE

in

ELECTRICAL ENGINEERING

December, 2015

Nashville, Tennessee

Approved:

Benoit M. Dawant, Ph.D.

Jack H. Noble, Ph.D.

To my parents,

and

And my siblings

ACKNOWLEDGEMENTS

CONTENTS

LIST OF TABLES

LIST OF FIGURES

CHAPTER 1

INTRODUCTION

1.1   Brief Overview

This thesis is divided into two sections in which two image processing techniques and associated analysis pertaining to the ear are presented.

The first section introduces a novel algorithm for segmenting the mastoid region to be drilled during acoustic neuroma surgery. This algorithm is built off of the commonly used atlas-based segmentation technique [1]. First, atlas-based segmentation is used to establish an initial registration. Following the application of the atlas-based segmentation, a series of refinements based around the landmarks in the ear are applied. These refinements consist of an inferior-superior depth refinement, a refinement based on a safety contour around the facial nerve, and a safety margin erosion. The erosion proved especially difficult because a global erosion could not be applied, requiring that a spatially adaptive erosion had to be developed instead. The resulting mastoid segmentation acts as an input to a bone-attached automatic bone drilling robot.

While acoustic neuromas are relatively rare constituting approximately 6% of all brain tumors, the surgery to remove one is extremely long and tiring [2]. The development of a bone attached automatic drilling robot can greatly decrease overall surgery time and benefit both the patient and the surgeon. In addition, the successful development of a bone attached

1

automatic drilling robot could be extended to other types of surgeries in which bone drilling is required such as mastoiditis and cholesteotoma surgery. However,the development of this robot has a variety of challenges associated with it. First of all, in the pathway to reach the acoustic neuroma, there are sensitive ear structures that must be avoided such as the facial nerve. There are also challenges associated with the placement of the robot on the skull. Lastly, there is a high level of variability in the shape and size of the mastoidectomy region due to differing patient anatomy.

The second technique presents a simulation model for electrode array insertion into the cochlea during cochlear implantation. Studies in the literature have shown that there is a high degree of variability in the placement of the electrode array in the cochlea following cochlear implant surgery and that this location of the electrode array within the cochlea impacts hearing outcomes [3, 4]. This section serves as a proof of concept study that developing patient-specific insertion plans could greatly improve the placement of the electrode array in the cochlea and thus potentially improve hearing outcomes post surgery. In this study we analyze the placement of the electrode array at a maximum insertion depth as recommended by the device manufacturer. We also analyze the placement of the electrode array when inserted at a shallower, more optimal depth. This analysis leads us to believe that there is a greater than expected variance between patient cochleas. Therefore, the development of patient-specific insertion plans using preoperative Computed Tomography (CT) scans could greatly improve the electrode array placement within the cochlea and result in more consistently improved hearing outcomes.

Although independent from each other, these two image processing techniques both address problems related to the ear. They both have the potential to positively impact surgery outcomes for the patient. They can do this by decreasing the time under surgery, decreasing the need for repeat surgery, and providing an overall better surgical outcome. However, they also have the potential to make the surgery easier and more consistent for the surgeon.

By decreasing surgery time for the surgeon, the risk of fatigue and mental mistakes also decreases. In addition, by providing a clear-cut plan for the surgeon to follow for a specific patient, the surgeon can have more confidence in the surgery they are completing. Overall, both of these methods, when proven safe and reliable, can greatly improve surgical efficacy.

CHAPTER 2

RESECTION PLANNING FOR ROBOTIC ACOUSTIC NEUROMA SURGERY

2.1 Keywords

Acoustic Neuroma, Atlas-based Segmentataion, Internal Auditory Canal, Cochlea, Facial
Nerve

2.2 Introduction/Purpose

Acoustic neuroma surgery is a procedure in which a benign mass is removed from the
Internal Auditory Canal (IAC). The IAC is a canal located in the temporal bone that serves
as the passageway for cranial nerves and is the location where acoustic neuromas form.
The location of the IAC is shown in Figure 2.1 (obtained from [5]) in which an IAC with
and without an acoustic neuroma are shown. Although benign, as this mass grows, it can
begin to press against the hearing and balance nerves in the head causing loss of hearing,
ear ringing, dizziness, and balance problems. Surgery is needed to remove the mass and
alleviate these side effects. The most commonly used acoustic neuroma surgery technique
is the translabyrinthine approach [6]. The translabyrinthine approach uses several different
steps to gain access to the IAC and remove the acoustic neuroma. First, a mastoidectomy
is performed in which both the mastoid region of the temporal bone shown in Figure 2.2
(obtained from [7]) and the semi-circular canals of the cochlear labyrinth are resected.
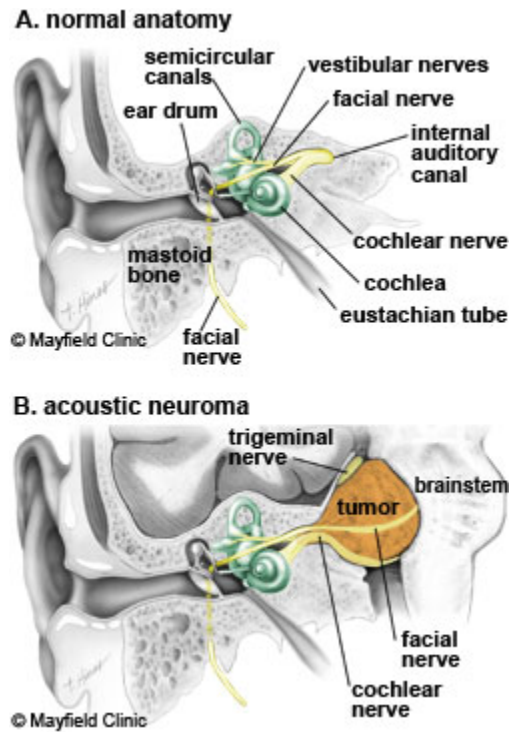
Figure 2.1: Inner ear anatomy showing development of the acoustic neuroma in the IAC
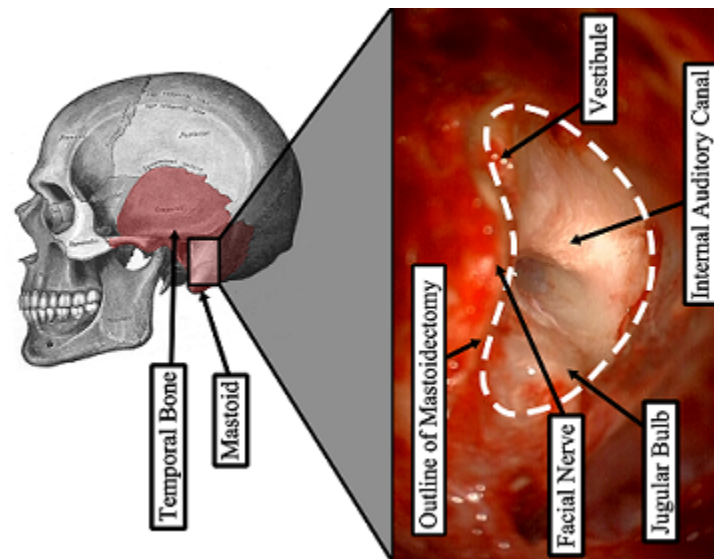
Figure 2.2: Region removed during the mastoidectomy and photograph from a surgical case with the corresponding sensitive ear structures exposed

This gives the surgeon access to the exterior bony wall of the IAC. After access to the exterior bony wall of the IAC is achieved, the bone is thinned until transparent so that the

location of the acoustic neuroma within the IAC can be visually identified. Finally, the acoustic neuroma is accessed and removed. The removal of the semicircular canals of the labyrinth results in hearing loss in the surgically altered ear. However, this is generally not a concern as the procedure is usually performed on patients with larger acoustic neuromas, meaning patients who have already experienced hearing loss. Additionally, this approach is generally preferred over other surgical approaches because it allows early identification of the facial nerve. This is vital as injury to the facial nerve can cause ipsilateral facial paralysis (paralysis of the facial muscles on the side of the face associated with the surgery). Early identification of the facial nerve allows the surgeon to maintain a safe distance from it while drilling.

The translabyrinthine approach puts several demands on the surgeon. The initial drilling step (the mastoidectomy) is physically taxing and can take two to three hours. In addition, the surgeon must be very precise during this portion of the procedure in order to identify and avoid damage to a number of sensitive anatomical structures that lie along the surgical path. The second step is also challenging. It is completed after the mastoidectomy when only a thin layer of bone is left covering the IAC. The surgeon must meticulously pick the thin bone away in order to gain access to the IAC. The first two steps increase the likelihood of fatigue, and thus mental mistakes, in the final portion of the procedure in which the acoustic neuroma is removed, which, depending on the patient's anatomy, can require a high degree of precision.

The Vanderbilt MED Lab is currently working toward the development of an Acoustic Neuroma Surgery Robot (ANSR) to perform the initial drilling procedure to gain access to the IAC. A prototype of the ANSR is shown in Figure 2.3 (obtained from [7]) . Future cadaveric studies may show that the ANSR is able to provide safe access to the IAC. If safe, the ANSR could greatly benefit the surgeon by decreasing the amount of physical and mental effort expended prior to the acoustic neuroma identification and removal step. This robot

may directly benefit patients as well by decreasing the total procedure time, and thus time under anesthesia, while maintaining the same levels of safety and efficacy as the traditional approach.
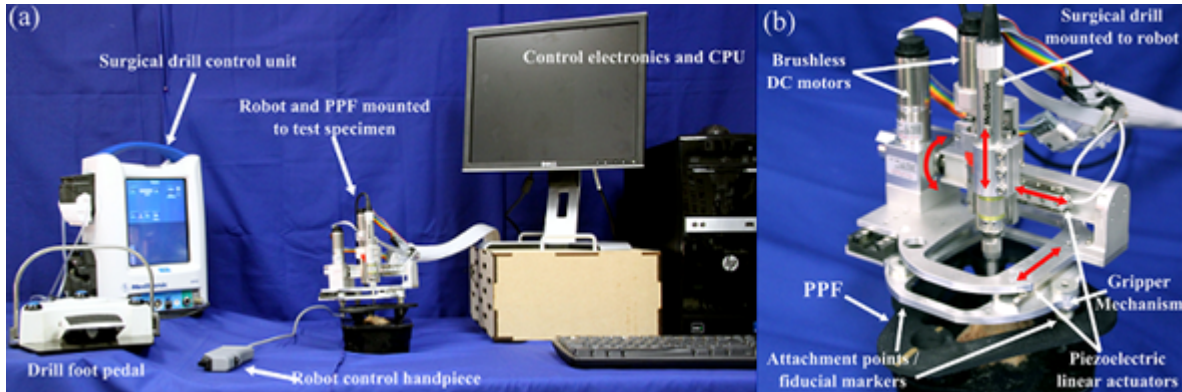
Figure 2.3: The ANSR prototype shown on the right along with the complete necessary set-up shown on the left.

In order for a robot to perform this drilling procedure, its path must be planned using pre-operative Computed Tomography (CT) images. This path must drill through the mastoid region and reach the IAC while avoiding vital structures such as the facial nerve. Once the region to be resected is defined, a complete set of instructions for the robot can be determined using drill path planning techniques that have previously been developed [8]. Currently, the drilling path utilized by the ANSR is manually delineated by the surgeon using 3D image segmentation software. But this is prohibitively time consuming (∼35 minutes) and requires care and expertise. In this work, we seek to develop an automatic approach for delineating the resection region using CT. We propose a multistep approach in which we first compute an atlas-based segmentation of the mastoid section of the temporal bone, refine it using anatomical landmarks, and finally apply a safety margin to the result producing a resection plan that requires only minimal editing by the surgeon. Automatic delineation of the resection region could lower the learning curve for surgeons who wish to adopt the ANSR approach and lead to more consistent plans across surgeons and patients.
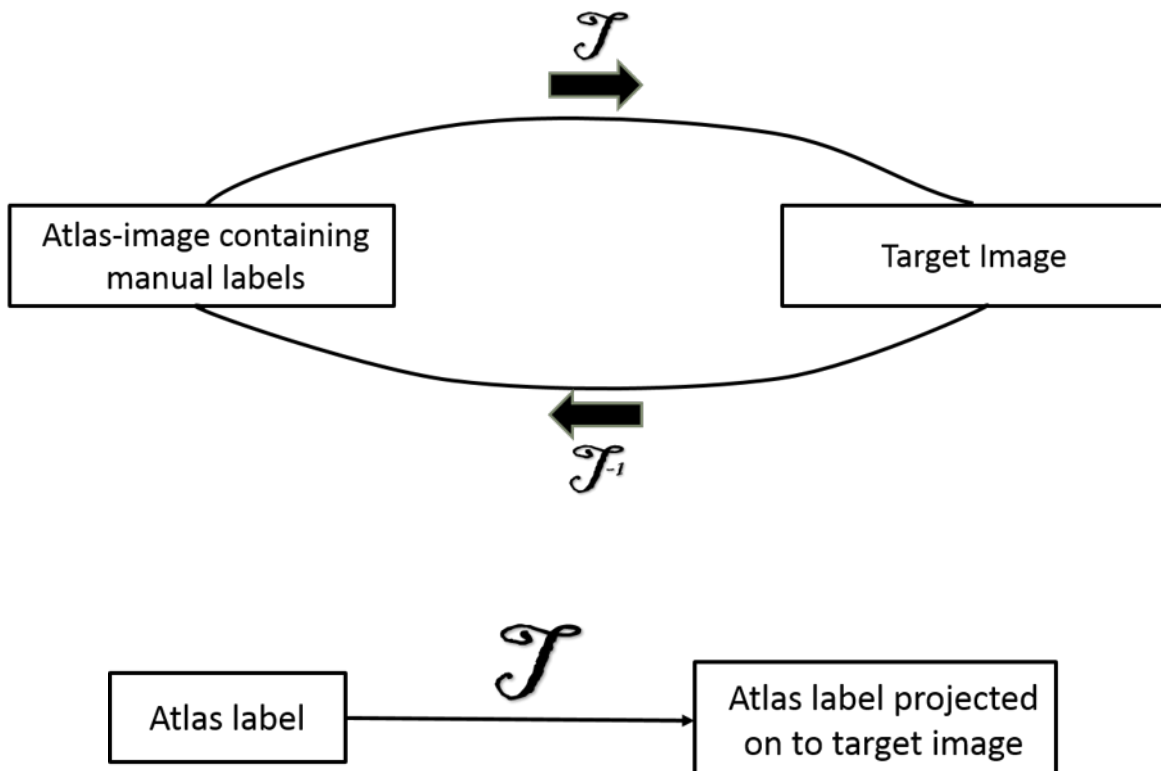
Figure 2.4: Visualization of atlas-based segmentation. The top figure shows the generation of correspondence (the transformation) between the known atlas image and the target image. The bottom figure shows that correspondence (transformation) being used to project the label in the atlas image onto the target image.

2.3 Methodology

Atlas-based segmentation is an approach in which manually labeled images, or atlases, are used to automatically label new target images. In this approach, one or more transformations are computed that register the atlas image to the target image [1]. Then the labels that are defined on the atlas are mapped to the target image using the registration transformations. This process is summarized in Figure 2.4.

Prior work from our group has shown that atlas-based segmentation techniques can be used to localize certain structures of the ear that have consistent topology and appearance
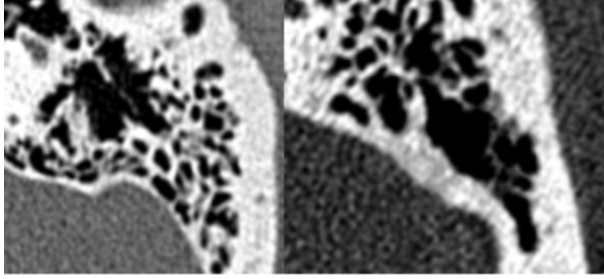
Figure 2.5: Different pneumatization patterns (the seemingly black holes within the white bone) in the resection region for two different bone specimens.

across different subjects [9]. However, the same techniques are not directly applicable to localization of the resection of volume of the ANSR. This is because the borders of the mastoidectomy lie within the temporal bone, which has a pneumatization pattern that is unique for each individual as shown in Figure 2.5. It is well known that atlas-based segmentation techniques are sensitive to such topological differences. This sensitivity makes atlas-based segmentation techniques inadequate for this application when used alone.

To account for these issues while still exploiting the atlas-based approach that was validated in prior studies, a multi-step atlas and landmark-based segmentation approach was developed. This approach is summarized in Figure 2.6. The first step is to segment the boundaries of the mastoid region of the temporal bone using atlas-based techniques [9] to serve as a coarse unedited segmentation of the resection region. The atlas-based approach relies on a sequence of linear and non-linear registrations computed between the target and an atlas image to automatically map a segmentation of the mastoid that was manually created in the atlas image to the target image volume using the compounded registration transformations. In our registration sequence, first an affine registration is computed to account for linear differences between images such as translation, rotation, scaling, and shearing. Following this, a local affine registration is computed around the region of the image containing the mastoid. This step improves the local registration accuracy. Finally, a local non-rigid registration is computed to account for non-linear differences between images such as stretch-

9

ing or dilation. Typically with an atlas-based approach, the borders of the segmentation in the atlas image are defined to match the Structure-Of-Interest (SOI), the planned region of resection in this application, as closely as possible. Our SOI has borders that fall within the pneumatized bone of the mastoid as shown in Figure 2.7 in blue. As mentioned previously, this poses a problem as registration in this area is often inaccurate due to inter-subject variability. To account for this, the initial segmentation volume in the atlas image is extended to follow the contours of the skull rather than the SOI itself as shown by the red contour in Figure 2.7. The exterior borders of the red contour are well identified in the target image via an atlas-based approach.
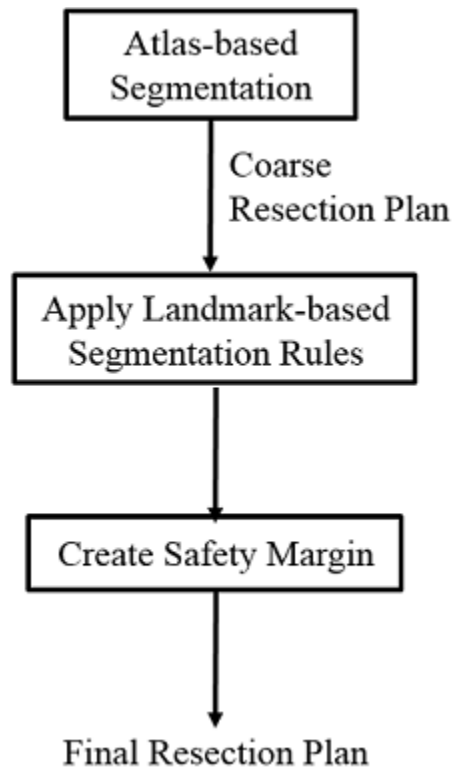
Figure 2.6: Condensed summary of steps performed to reach a final resection plan

The next step is to refine the borders of the initial segmentation using a landmark-based strategy based on the decisions the surgeon typically makes during surgery. This first requires segmenting the IAC, labyrinth, and facial nerve to serve as landmarks. The IAC

10
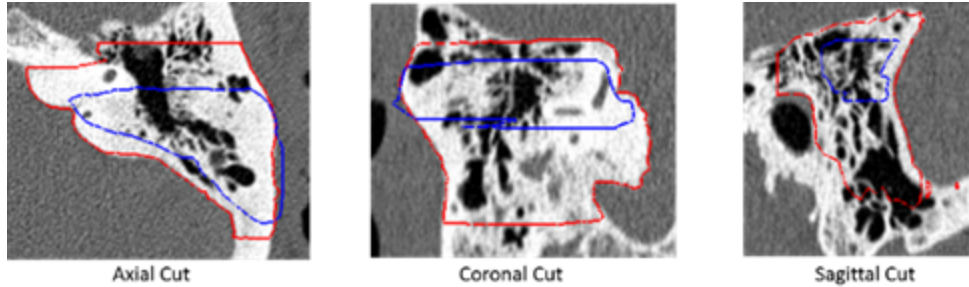
Figure 2.7: Comparison between surgeons manually delineated resection plan (blue) and the segmentation of the full mastoid region of the temporal bone (red) that is used in our atlas-based segmentation step.

is localized using atlas-based techniques [9] and the labyrinth and facial nerve are localized using techniques we have previously developed and validated [10, 11]. To refine the superior boundary of the SOI, the SOI is edited so that no tissue is resected superior to the labyrinth. The superior boundary can be defined as a simple axially-oriented plane, while the inferior boundary must be defined as a slanted plane (see Figure 2.8). This is so that the inferior boundary of the IAC can be reached while also allowing the SOI to expand inferiorly away from the IAC as it approaches the lateral surface of the skull to permit adequate access for surgical tools necessary for the removal of the acoustic neuroma. To do this, a plane is defined that contains the most inferior point on the IAC segmentation and two points on the mastoid tip. The SOI is then automatically updated so that no tissue is resected inferior to this plane.

Next, the anterior boundary of the SOI is updated to ensure the anterior border of the IAC can be reached while remaining posterior to the facial nerve and the portion of the labyrinth that cannot be resected (see Figure 2.9). As mentioned previously, the semicircular canals of the labyrinth are removed during the manual drilling portion of the surgery. While their removal is unavoidable, it is preferred to only remove portions of the labyrinth needed to gain access to the IAC. In order to define which portions of the labyrinth cannot be drilled, the vertices of the labyrinth that are allowed to be drilled versus those vertices that cannot

11
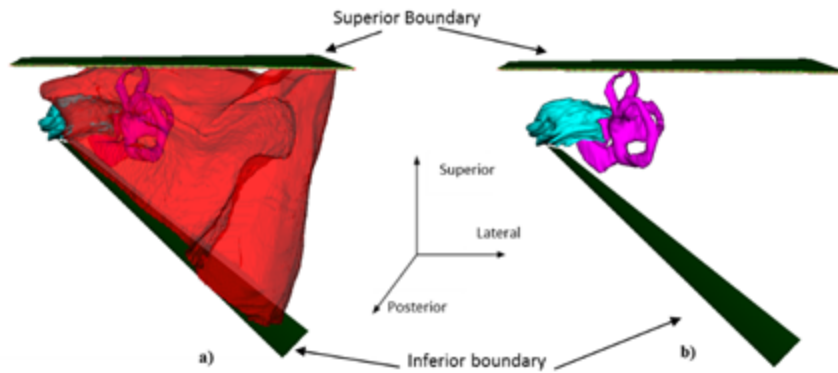
Figure 2.8: The superior and inferior resection boundaries shown a) with the automated resection surface included and b) with the automated resection surface removed. The IAC is shown in cyan, the labyrinth is shown in magenta, and the automated resection surface is shown in red.

be drilled are labeled in the atlas labyrinth surface based on the surgeon's recommendations. The labyrinth surface is segmented in the target image using a model-based technique that results in a one-to-one point correspondence between the atlas and target surface vertices. Automatically defining the vertices in the target labyrinth that should not be drilled is done by simply using the same labels defined in the atlas. Figure 2.10 shows the two labels as defined by the surgeon.

To define a 0.5 mm safety margin of bone around the facial nerve that cannot be drilled, a three-dimensional distance map is computed for the facial nerve. In each axial slice, isocontours are computed from the distance map 0.5 mm from the facial nerve. An example slice of this contour as well as its 3D representation is shown in Figure 2.11. Due to the complex spatial relationship of these structures, updating the anterior boundary of the SOI to ensure it does not violate the facial nerve safety margin or the portion of the labyrinth that cannot be resected cannot be done using edits defined by simple planar geometry. We thus define a decision contour in each axial plane and automatically adjust the SOI so that no tissue is resected anterior to the decision contour in that axial plane. The contour (an
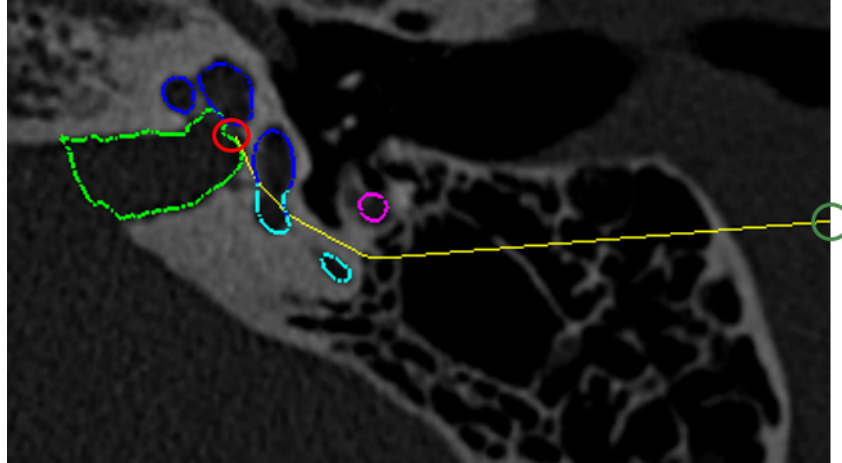
Figure 2.9: Example of final line segment (shown in yellow) for one slice. The IAC is shown in light green, the facial nerve is shown in pink, and the labelled labyrinth is shown in dark blue and light blue. The initial point on the IAC is indicated by the red circle. The end point is indicated by the dark green circle.
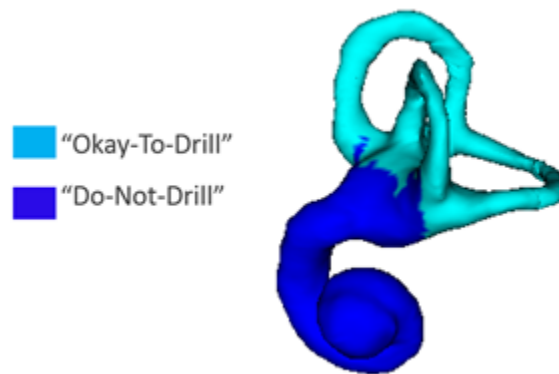
Figure 2.10: Labyrinth labels designating the portion of the labyrinth that should and should not be drilled based on the surgeons recommendations

example is shown in yellow in Figure 2.9) is composed of a series of line segments that are dependent on the points of the labyrinth that cannot be drilled as previously discussed as well the isocontour points. More specifically, it is defined as the shortest convex path that connects the most anterior point of the IAC to the most posterior point on the facial nerve safety margin isocontour. While doing this, it must pass posterior to the facial nerve isocontour and the portions of the labyrinth that cannot be resected. Once the contour
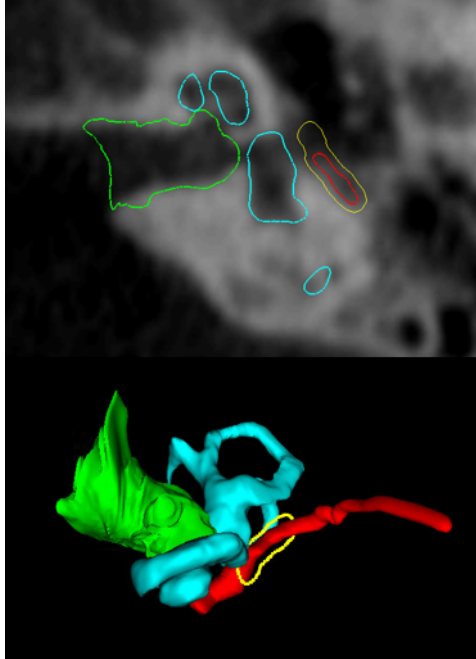
Figure 2.11: Example of the safety contour (shown in yellow) around the facial nerve (shown in red). The safety contour shown is for only one slice. The labyrinth is shown in light blue and the IAC is shown in green. The top figure shows the corresponding CT slice and the bottom shows the 3D surfaces.

reaches the most posterior point on the facial nerve isocontour, it is extended laterally to the surface of the skull. The path is constrained to be convex to avoid defining a contour that has concavities that could complicate drilling. A common issue when analysis is performed slice-by-slice in this fashion is that it produces an irregular 3D shape. However, this issue is avoided here because the contours are constructed based on smooth 3D landmarks. The posterior border of the SOI does not need to be refined as it is well-defined already by the border of the skull-brain interface. The following is a vector mathematical breakdown of this algorithm. First we combine the labyrinth label points and the isocontour points (our decision contour) into a matrix represented by PD where the size of the matrix is determined by the number of contour points for that particular slice (N). The points in the decision contour matrix are in no particular order Next, the point of interest is defined as PI. Our first point of interest will start as the initial point which is chosen as the most anterior

lateral point on the IAC. PI will change throughout the algorithm application based on the decision contour. The end point, which will not change throughout the algorithm, is defined as PE and is chosen to be the most posterior point in the facial nerve contour extended laterally to the most lateral edge of the mastoid These variables are described below.

$$Slice\# = PE_z = PI_z = PD_z \tag{2.3.1}$$

$$P_D = \begin{pmatrix} PD1_x & PD1_y \\ PD2_x & PD2_y \\ . & . \\ . & . \\ PDN_x & PDN_y \end{pmatrix} \tag{2.3.2}$$

$$PI = (PI_x, PI_y) \tag{2.3.3}$$

The ideal path between PI and PE is a straight line: PIE, but our decision contour points change this path so that the facial nerve will not be drilled. To account for this, a vector normal to PIE is defined as N_{hat} shown below.

$$PIE = \frac{PE - PI}{|PE - PI|} \tag{2.3.4}$$

$$N_{hat} = (PIE_y, -PIE_x) \tag{2.3.5}$$

Next the displacement vectors from PI to the points in the decision matrix are defined as V_k where k = 1:N. All the displacement vectors are then projected onto N_{hat} and defined as $Proj_k$ again where k = 1:N. These equations are shown below. To meet the requirements that no portion of the bone anterior to the decision isocontour will be included in the drilling

15

region, points corresponding to a negative projection are automatically not considered for the line segment.

$$V_k = PDk - PI$$
$$k = 1 : N$$

(2.3.6)

$$Proj_k = \frac{V_k \bullet (N_{hat})}{|V_k|}$$

(2.3.7)

The point with the largest displacement vector projected onto N_{hat} then becomes the next point of interest (PI) as indicated by the equations below.

$$PI = PDj$$
$$j = argmax_k(Proj_k)$$
$$k = 1 : N$$

(2.3.8)

Thus by choosing the test point with the larger corresponding projection onto N_{hat}, the most posterior points in the decision contour matrix will be chosen. This ensures that the line segment that is generated for each slice will not include any portion of the bone that violates the labyrinth label or the safety isocontour around the facial nerve in the drilling region. This also ensures that the anterior line segment that is generated will always be convex as mentioned previously. This algorithm is pictorially visualized in Figure 2.12 where only the $argmax(Proj_k)$ and its corresponding displacement vector are shown.

Finally, to account for the fact that surgeons typically desire a 1 mm margin of bony tissue to not be drilled at the borders of the resection region and to account for up to 1 mm of error in the drilling system, we apply an erosion to the SOI. A simple global erosion using a spherical structuring element (SE) in this case is not desirable as the lateral wall of the SOI on the mastoid is where the ANSR will begin drilling and must not be eroded. Instead, a spatially adaptive structuring element (SASE) is used. The SASE must be a full sphere for
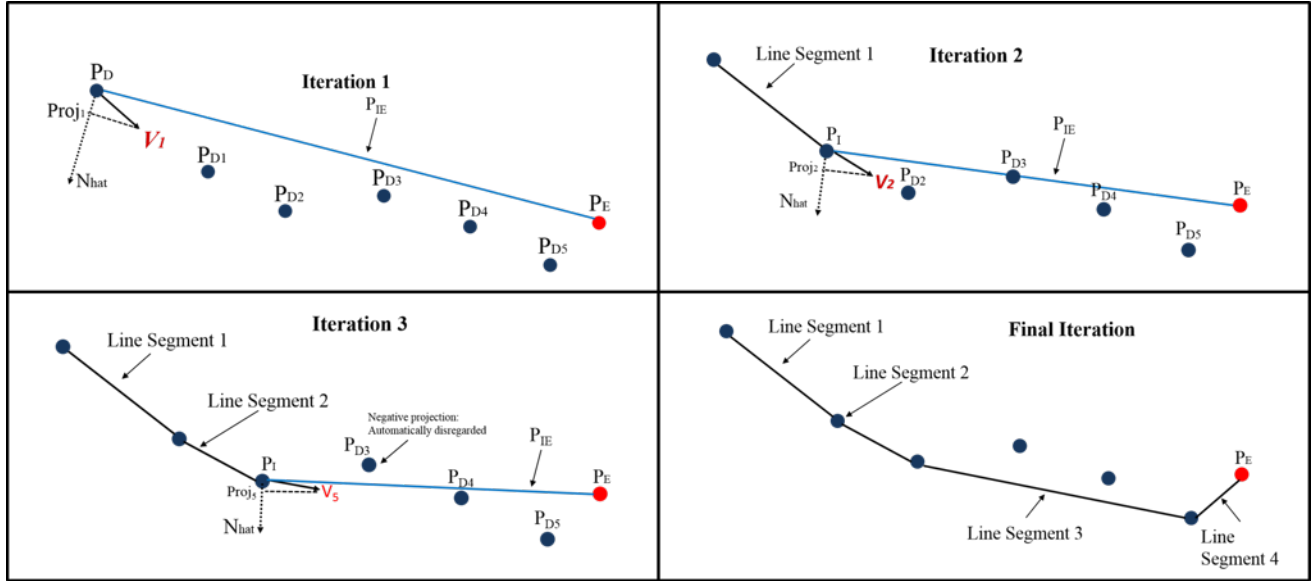
Figure 2.12: Visualization of algorithm through five iterations. Iteration three shows how a negative projection is handled in the algorithm.

most of the SOI to ensure safety but should be a medial-facing quarter-sphere at the lateral edge of the SOI to prevent eroding the border of the SOI at the lateral surface of the skull (see Figure 13).

Rather than defining the SASE to sharply transition from full to partial sphere, the SASE is designed to vary smoothly over the image space so that the final resection plan will be smooth. The spatial adaptation function, i.e., the function that defines the shape of the SASE based on spatial location, cannot be defined using simple planar geometry due to the contoured shape of the skull. Instead, the spatial adaptation function is defined using a radial basis function network approach. To do this, first, a surface defined around the initial segmentation volume in the atlas image is projected onto the target image through the compound registration transformation. Figure 2.13 shows an axial slice of a target image with the cut of the axial slice through this surface shown as the blue, cyan, and yellow contour. Each vertex in the original surface in the atlas image is classified into one of three groups, vertices in a region that requires a full spherical SE (cyan), those in a region that

17
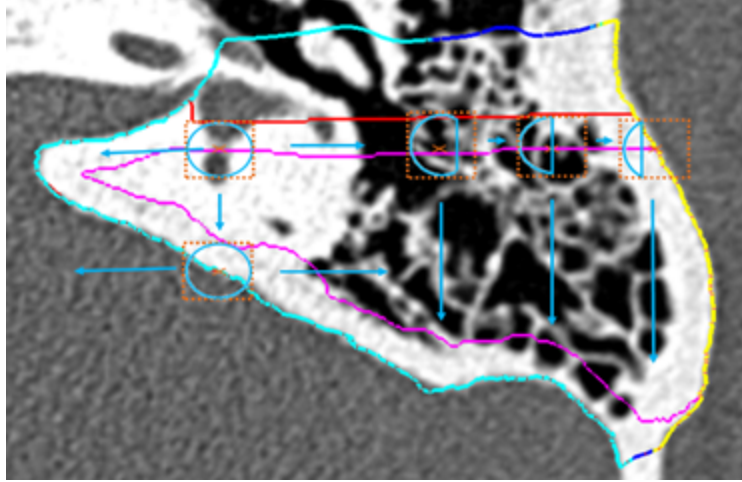
Figure 2.13: The spatially adaptive structuring element (SASE) process. Light blue circles show the SE that is being used for the voxel of interest (orange x). Dashed orange box surrounding the SE shows the range of the SE. The initial mastoid segmentation surface is shown in cyan, blue, and yellow. The resection plan prior to erosion is shown in red and the resulting resection plan after erosion is shown in magenta.

requires a quarter spherical SE (yellow), and those that fall between these two regions (blue). These vertex classifications are then identically mapped to the corresponding vertices in the target surface. The colors of the contour in Figure 2.13 show an example result of this process. Next, a Gaussian radial basis function $G_{\sigma,v_i}(x, y, z)$ is defined in the target image at the location of each ith surface vertex v_i in the group of N vertices that are classified in the cyan or yellow groups. Finally, the spatial adaptation function can be defined using the network of radial basis functions as

$$D(x, y, z) = \frac{\sum_{i=1}^{N} D_i G_{\sigma,v_i}(x, y, z)}{\sum_{i=1}^{N} G_{\sigma,v_i}(x, y, z)} \tag{2.3.9}$$

where σ is selected to be 2 mm, D represents the fraction of the sphere of the SE associated with v_i and is equal to 1 for the cyan group and 0.25 for the yellow group, and D(x,y,z) defines the fraction of the sphere that we select to be used for the SE at location x,y,z in the target image. In summary, the shape of the SE is defined by Equation 2.3.18 as a weighted average

of the SE shape defined at sites around the initial segmentation surface, where weights are selected based on the distance to each site. The SOI volume that has been refined using the landmark-base scheme described above (shown as red contour in Figure 2.13) is eroded using the SASE with a radius of 2 mm (shown as cyan SEs in the figure) to add a safety margin and account for targeting error, resulting in a final automatic resection volume (shown as magenta contour in the figure). Note that while the spatial adaptation function in equation 2.3.18 is defined-based on the initial segmentation surface (multicolored contour), it is a 3D function and thus can be used to apply the SASE to erode the refined (red contour) rather than the initial segmentation.

To validate the safety of the automatic resection plan, first, the surgeon manually delineated a maximum safe drilling volume from scratch for each patient, without benefit of the automatic resection plan. Then, the percentage of voxels of the automatic resection plan located inside the manually defined maximum drilling volume was calculated. Some difficulty was encountered in defining a truly maximum drilling region due to discrepancies between the region that is typically drilled in surgery and additional regions that may not always be resected but are still safe to drill. In addition, there are some difficulties in precisely defining a 3D volume by manually delineating a sequence of 2D slices. To account for this, any voxels in the automatic plan that were located outside the maximum drilling region were then examined by the surgeon and further labelled as safe or unsafe. To verify that the automatic resection plan is functional, the surgeon was instructed to make any adjustments to the automatic resection plan that would be required so that when the ANSR finishes, the surgeon would need only to thin the bone around the IAC to reach the acoustic neuroma and would be provided adequate working space to do so. The adjusted plan was then compared to the automatic plan using surface distance measurements and Dice Similarity Coefficient (DSC) [12].

2.4 Results

This segmentation procedure was performed on 9 separate CT scans: 4 patients and 5 cadavers. Results are shown in Table 2.1.

Patient	1	2	3	4	5	6	7	8	9	Mean (Worst Case)
% Within Maximum	99.07	95.46	98.79	99.06	97.92	92.98	90.96	93.57	98.61	96.27 (90.96)
Verified Safe	Yes	Yes	Yes	Yes	Yes	Yes	Yes	Yes	yes	N/A
Max Surface Error (mm)	1.88	1.96	2.74	4.98	3.84	1.73	2.63	3.11	1.29	2.69 (4.98)
Mean Surface error (mm)	0.04	0.05	0.09	0.09	0.17	0.09	0.06	0.10	0.06	0.08 (0.17)
Dice Coefficient	0.99	0.99	0.99	0.99	0.97	0.99	0.99	0.97	0.99	0.99 (0.97)
Time to edit automatic plan (min)	03:00	01:48	03:00	02:19	06:02	01:58	02:15	02:38	02:08	2:08 (06:02)

Table 2.1: Quantitative validation results for automatic resection plans.

A mean of 96% of resection plan voxels were found to be within the maximum region. Notice that the lower amount of voxels found within the maximum region are for the cadaver images (6-9). This is most likely a result of a decrease in image quality as compared to the patient scans, which made it more difficult to manually identify a maximum region and to generate an automatic resection plan due to a decrease in registration accuracy. The few voxels that were located outside the maximum for each patient were examined, and these were verified by the surgeon as voxels that could still be safely drilled. Good agreement is seen between automatic and adjusted surfaces with small mean and max surfaces errors of 0.08 and 2.69 mm and high average DSC of 0.99 on average. A 3D rendering of two of our resulting surfaces that correspond to the best and worst DSC (cases 9 and 4) are shown in Figure 2.14 and 2.15 respectively. In the figure, the automatically generated resection plans

are color-mapped with distance to the border of the adjusted plan. The highest errors occur medially or around the IAC, indicating that our plan was conservative in this region
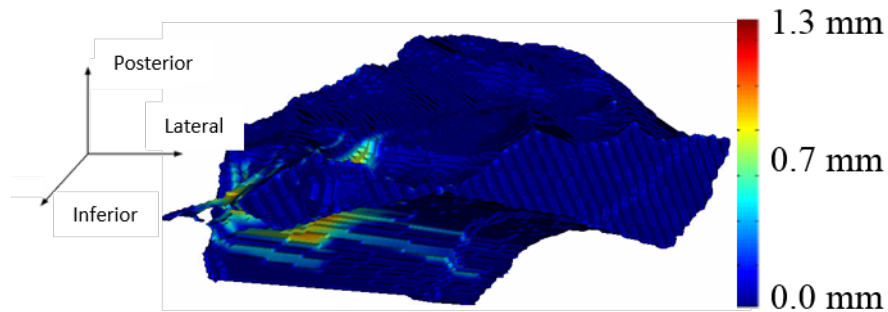
Figure 2.14: Resection plan for best case color-mapped with error distance.
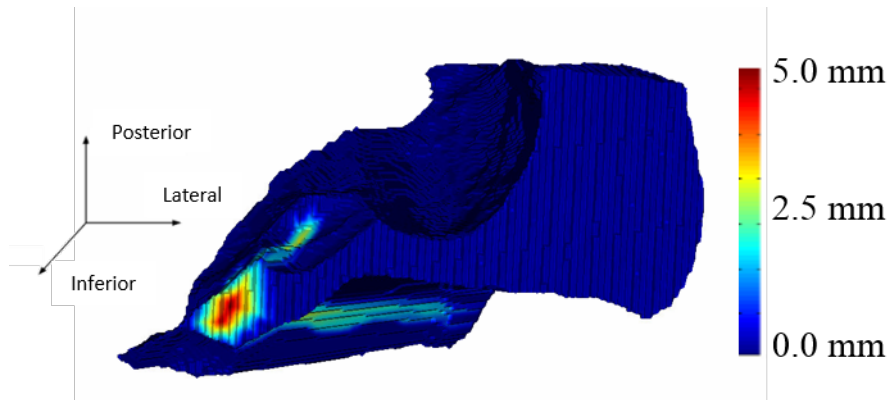
Figure 2.15: Resection plan for worst case color-mapped with error distance.

2.5   Conclusions

In this study, we present the first approach for automatically determining patient-specific resection plans for acoustic neuroma surgery. Another group has developed techniques for segmentation of the borders of the mastoid [13]. Our approach is distinct in that it aims to identify a drilling region within the mastoid. Our approach was verified to be safe in every case. Previously, the superior portion of the automatic resection plan was that most edited by the surgeon which was needed to allow functional access to the IAC. This was

addressed by expanding the superior border of our SOI in our atlas. In all cases, the surgeon edited the resection plan to move its border closer to the IAC. Because this goes beyond the limits defined for the automatic approach to maintain adequate margins for safety and to account for targeting error, this type of edition cannot be done automatically. However, editing the automatic plan only required an average of 2 minutes of work by the surgeon, which represents a drastic reduction in required effort compared to manually planning, which requires an average of 35 minutes. In all instances where edits were made, the surgeon was increasing the drilling volume. This shows that our plan was overly conservative rather than unsafe, which is preferred.

CHAPTER 3

PATIENT-SPECIFIC SIMULATION OF COCHLEAR IMPLANT ELECTRODE ARRAY
INSERTION TECHNIQUES

3.1 Keywords

Cochlear Implant Surgery, Internal Auditory Canal, Cochlea, Scala Tympani, electrode array, angular depth of insertion, millimetric depth of insertion, round window, cochleostomy

3.2 Introduction/Purpose

A cochlear implant is a surgically implanted neural prosthetic device used to restore hearing sensation in patients with profound hearing loss [14]. The device is composed of an electrode array which stimulates the auditory nerve once it has been implanted into the cochlea. Implantation into the cochlea is generally achieved one of two ways: via a round window (RW) insertion or a cochleostomy (CO) insertion [15]. The round window is located between the middle ear and the inner ear and is one of two openings at that location. During a round window insertion, the electrode array is inserted into the cochlea through the round window membrane. A cochleostomy insertion consists of first drilling an opening into the cochlea inferior to the round window. Once this hole has been drilled, the electrode array is then inserted through this opening into the cochlea. After insertion into the cochlea has successfully been achieved using one of the two insertion methods, the surgeon threads the

electrode array in the scala tympani (ST). The ST is a cavity within the cochlea and is shown in Figure 3.1. Some electrode array models are straight, but there are also several electrode array models that come pre-curved. If the electrode array is pre-curved, it is accompanied by a straightening stylet. The straightening stylet allows the surgeon to advance the electrode array off of the stylet and into the ST. As the electrode array is advanced off of the stylet the shape of the array is intended to match the shape of the ST. This approach is known as the Advance-Off-Stylet (AOS) technique. The electrode array is advanced off the stylet into the cochlea until a marker at the base of the electrode array reaches a desired location at the opening of the cochlea. The AOS technique helps facilitate less traumatic placement of the array within the ST as it is less reliant on the walls of the ST to guide the electode array into the cochlea compared to straight electrode arrays [16, 17].

Recent studies have shown that the electrode array's placement within the cochlea can be highly variable from individual to individual. In addition, certain factors related to the electrode array's placement within the cochlea such as scalar location, have been found to be correlated with hearing outcomes [3, 4]. Holden et al. showed that placement of electrodes closer to the modiolus, as is facilitated by pre-curved electrode arrays, is linked with better outcomes [18]. Achieving perimodiolar placement within the cochlea also appears to reduce power consumption and give longer battery life to cochlear implant patients. Poorer hearing outcomes have also been associated with placing the electrode array too deeply into the cochlea [18, 19, 20]. However, poorer hearing outcomes have also been associated with an electrode array insertion depth that is too shallow [21, 22]. A recent study by our group has further shown that it is possible to select patient-specific programming parameters that mitigate some of the effects of sub-optimal electrode placement on hearing performance [23, 24]. Overall, there is an abundance of evidence supporting the fact that the electrode array's position within the cochlea affects hearing outcomes. Therefore, identifying an ideal electrode array placement location could result in better hearing outcomes for cochlear implant

patients. The literature shows that on average pre-curved electrode arrays are positioned closer to the modiolus than straight electrode arrays [25]. However, even pre-curved electrode arrays are not typically positioned perfectly against the modiolus [25]. Improving the placement procedure of pre-curved electrode arrays could prove significant. In addition, better insertion techniques could reduce the amount of trauma to the ST that often occurs from the electrode array's interaction with the walls of the ST. The goal of this study is to analyze surgical placement techniques in simulation to determine whether any optimizations to the placement procedures for pre-curved electrode arrays can be introduced. Our approach is to analyze simulated placement of the electrode arrays using three dimensional models of pre-curved electrode arrays and models of the ST reconstructed from CT images of a number of individuals.

Other groups have developed biomechanical physics-based simulations designed to simulate the path of the electrode array into the cochlea as it interacts with the walls of the cochlea through deflection and frictional forces [26, 27, 28]. A limitation of these types of simulations is that the accuracy of the electrode array model cannot be verified, and thus the results may not be realistic. Other studies have reported on behavior of real electrode arrays as they are inserted into a single synthetic ST model [17]. The limitation of this type of study is that the ST model does not capture typical shape variations seen in the ST across individuals. The quantitative analysis we present in this study accounts for ST shape variations and makes no assumptions about the shape the electrode array will take after interacting with the walls of the ST. Our approach is to compare the shape of the ST chamber of a number of individuals with the trajectory of the electrode arrays as they are advanced off the stylet in air, without being perturbed by interactions with the ST for both a round window and a cochleostomy insertion approach. A closer match between the shape of the ST and the electrode array trajectory would indicate that less physical interaction

between the electrode array and the walls of the ST would be required during the insertion procedure, leading to decreased trauma.

3.3   Methodology

Our first step in creating our simulation model was to acquire an experimental dataset. This required extracting examples of ST geometry from patient CTs and then constructing trajectory models of the Contour Advance (CA), which is manufactured by Cochlear Corporation, Inc. (Melbourne, Australia), and the Mid-Scala (MS), which is manufactured by Advanced Bionics, LLC. (Valencia, California, USA). This was done using practice electrode arrays provided by the aforementioned companies. We utilized the CT's of nine individuals. For each individual's CT, we acquired the ST using methods previously developed which accurately localize the ST surface [29]. Our goal was to simulate electrode array insertion into the ST for both types of electrode arrays. For each electrode array type we also aim to simulate both the RW and CO insertion methods for each ST. To do this, a RW and a CO entry point into the ST were selected manually. These entry points are shown in Figure 3.1. The angle of the entry trajectory is also defined by the points in Figure 3.1 and represent the depth of insertion of the tip of the stylet when performing the AOS procedure for CA and MS electrode arrays, selected based on the depth implied by the position of the AOS marker on these electrode arrays.

To create trajectory models for both the CA and the MS electrode arrays a group of practice electrode arrays were used. For each practice electrode array the stylet was retracted starting at 0 mm until it was fully removed from the electrode array. The practice electrode arrays with the stylets retracted by different amounts are shown in Figure 3.2.

The exact amount of stylet extraction was measured using digital calipers under a microscope. A 3D reconstruction of each of these electrode arrays was then performed by localizing the position of each contact in a CT scan that was acquired of the electrode arrays. This
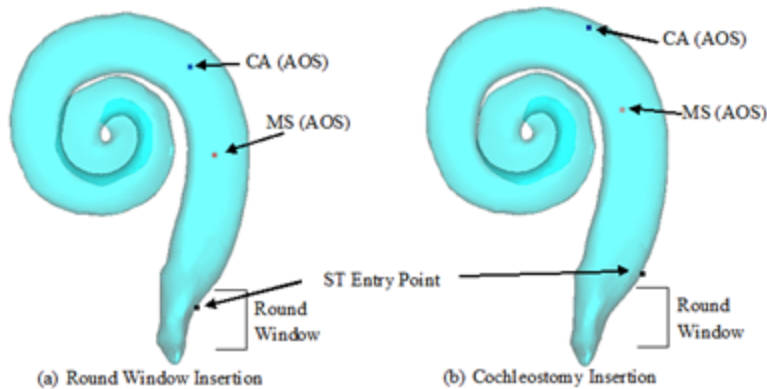
Figure 3.1: A representative scala tympani in our dataset is shown with entry points selected for simulating both RW (a) and CO (b) insertions. Also shown are points representing stylet position for the AOS procedure. The depths of the stylet position points are selected based on the AOS marker position on the array for each model.

3D reconstruction is shown in Figure 3.3. Each 3D reconstruction of the electrode arrays is color-coded to represent the amount of stylet extraction in millimeters.

In Figure 3.3, the 3D reconstruction of each electrode array is aligned such that the tip of the stylet is co-located across electrode arrays. The shape of the electrode array at the largest retraction amount is equivalent to the final relaxed shape of the electrode array with the stylet completely removed. Using the 3D reconstructions of the practice arrays we are able to simulate the shape of the electrode array for stylet retraction amounts that are located in between our samples retraction amounts. This is done by interpolating a weighted average between shapes. In order to estimate the millimetric insertion for a speific electrode array that is not included in our model we use interpolation. During the interpolation process, the electrode arrays are treated as a sequence of linear segments attached at joints. That is to say that each electrode position in the electrode array is treated as a joint between line segments with joint angles that specify the angles between the line segments. Then to interpolate the new shape the joint angles between the known electrode arrays are linearly
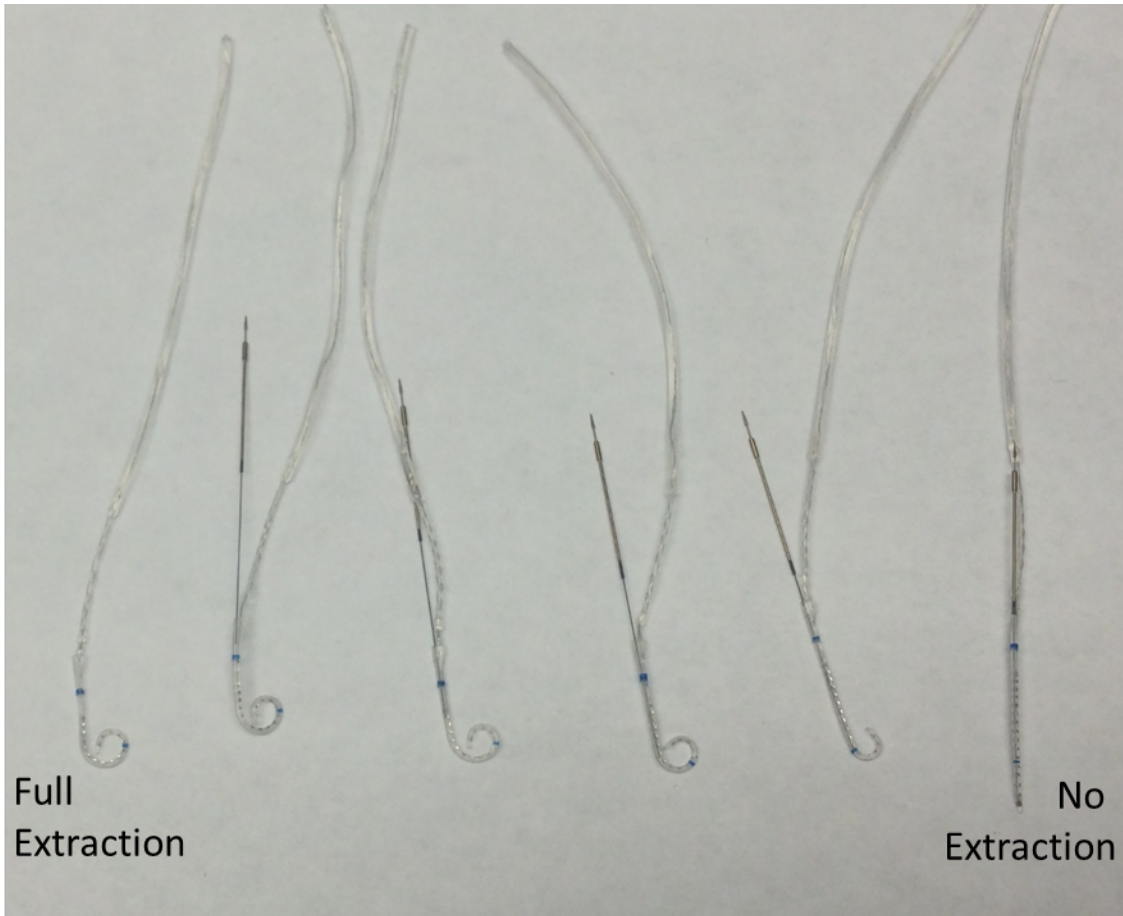
Figure 3.2: Practice electrode arrays with the stylet extracted by diffferent millimetric amounts starting a 0mm and ending when the stylet is fully removed.

interpolated as mentioned previously. Using this scheme, the trajectory of an electrode array as it is advanced off the stylet can be simulated by iteratively estimating the shape of the array while increasing the amount of stylet retraction from 0 mm to fully retracted.

Using the above ST models and electrode array trajectory models, we simulate patient-specific insertion trajectories and analyze variability in AOS position. As part of this analysis we measure the variability in angular AOS depth. The angular depth of a position within the cochlea is defined by measuring the angle of that position around the mid-modiolar axis relative to the center of the RW, which defines the 0 degree angular position as shown in Figure 3.4, where 90 degrees relative to the mid-modiolar axis is also shown. This convention
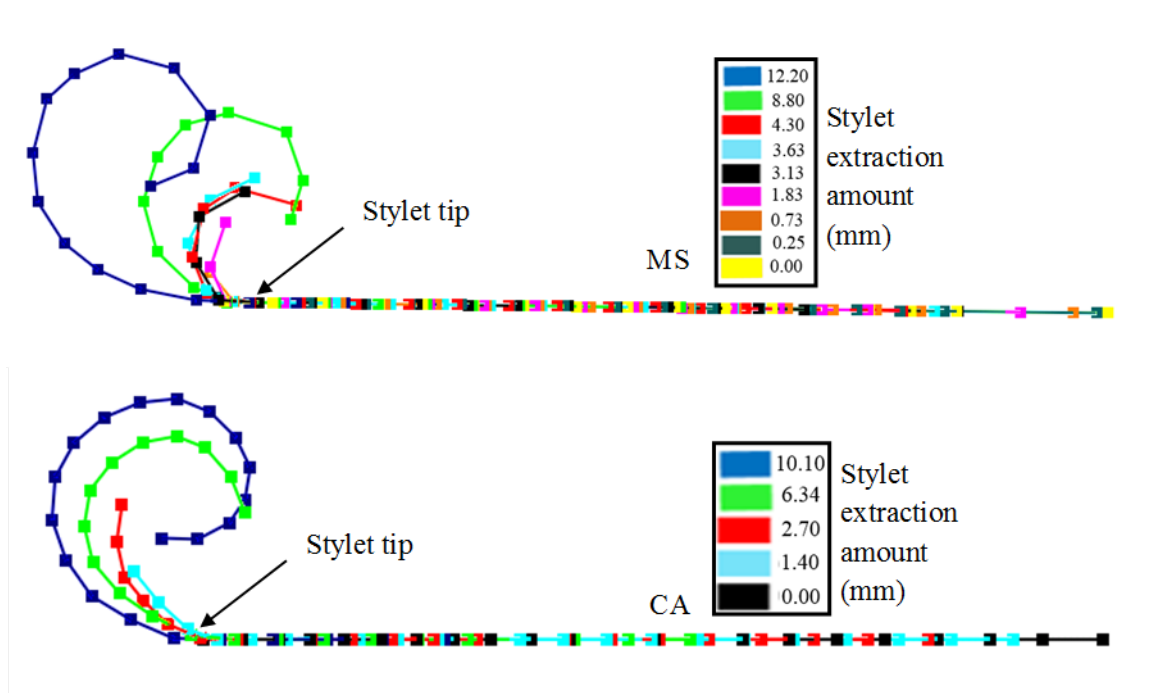
Figure 3.3: Resting state shapes of the Mid-Scala (MS) and Contour Advance (CA) electrode arrays in air measured in CT images with the stylet extracted by different amounts. These electrode array samples are used to create a shape model for the MS and CA electrode arrays

was established by Verbist et al. [30]. The variability in angular AOS (aAOS) depth is measured by fixing the millimetric AOS depth (mAOS) and then measuring the corresponding aAOS depth across different STs. This is done by aligning the AOS marker on the CA and MS electrode arrays with the RW.

Additionally, the variability in mAOS depth is measured by fixing the aAOS depth across individuals. However, obtaining a specific aAOS is not currently possible clinically due to the variability in ST geometry. Anecdotal reports suggest that recommended aAOS depths for CA and MS electrode arrays are approximately 90 and 60 degrees, respectively.

As mentioned previously, in order to analyze patient-specific insertion trajectories, the electrode array shape models were aligned with each ST surface using a manually determined entry point and stylet position (shown in Figure 3.1). Then the model was used to estimate
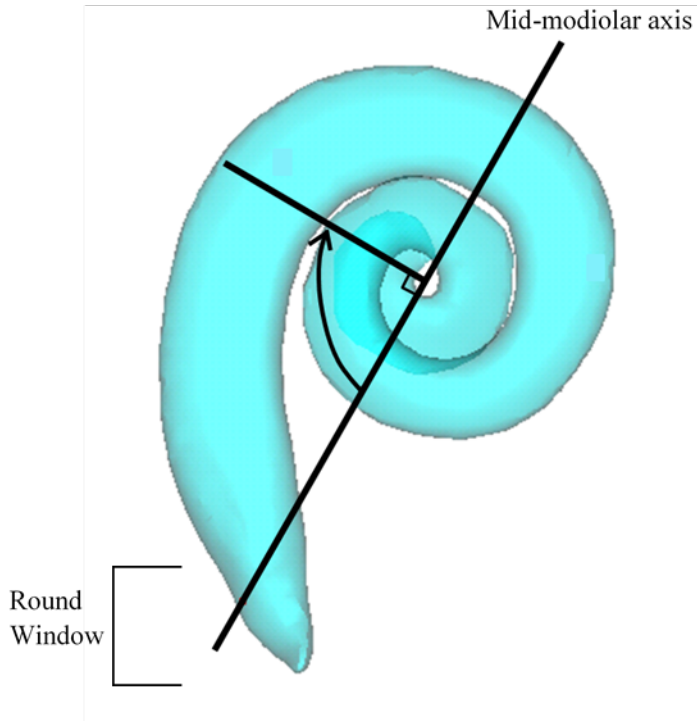
Figure 3.4: Axis of measurement for angular insertion.

the insertion trajectory as the electrode array is advanced off the stylet. In order to quantify the insertion quality, the distance between the insertion trajectory and the optimal trajectory of the electrode array in the ST is computed. The optimal trajectory of the electrode array into the ST was defined as the trajectory that follows the central axis of the ST for MS electrode arrays. The optimal trajectory into the ST for CA electrode arrays was defined as the trajectory that hugs the modiolar wall of the ST. Optimal trajectories were found by applying central axis extraction techniques on the ST surface [31]. Following this extraction, the resulting curves were edited to match the central axis of the ST for MS electrode arrays and to hug the modiolar wall of the ST for CA electrode arrays. This was done using in house 3D editing software. The simulation of the electrode array insertion was completed in time steps. Each electrode array was progressively advanced off the stylet from 0 mm in steps of 0.05 mm until the full depth of insertion was reached. For each time step of

30

ST	aAOS (degrees)		mAOS (mm)	
	MS	CA	MS	CA
1	73	90	4.94	6.49
2	78	95	4.59	6.45
3	69	91	4.86	6.51
4	56	73	5.62	7.03
5	86	130	4.35	6.04
6	55	113	3.86	5.99
7	50	85	5.38	7.09
8	60	88	4.35	6.93
9	50	89	5.96	7.38
Mean	64	95	4.88	6.66
std	13	17	0.68	0.48

Table 3.1: Results obtained measuring aAOS and mAOS depths across subjects.

the simulation, the average and maximum distances between the insertion trajectory and the optimal electrode array tractory is computed. This allowed the insertion quality to be visualized by plotting the distance between the simulated insertion trajectory and the optimal array insertion trajectory as a function of the distance the electrode array has been advanced off the stylet.

3.4 Results

The variability in aAOS and mAOS measurements found from fixing mAOS and aAOS depth repectively are shown in Table 3.1.

The aAOS columns correspond to the angular position of the most apical electrode in each ST when inserting the electrode array until the AOS depth marker reaches the RW. We measure average aAOS depth of the most apical electrode in MS and CA electrode arrays to be approximately 64 and 95 degrees, respectively. The standard deviation aAOS depth of both electrode arrays is larger than 10 degrees, and both electrode arrays have a range in aAOS of around 50 degrees. The mAOS columns correspond to the millimetric depth of the

31

most apical electrode when using a fixed angular AOS depth of 60 and 90 degrees for the MS and CA electrode arrays. We measured the average and standard deviation of mAOS depth to be 4.88±0.68 mm for the MS and 6.66±0.48 mm for the CA electrode arrays. The MS and CA electrode arrays have a mAOS range of 2.1 and 1.4 mm, respectively. These data suggest 1.5-2 mm differences in mAOS corresponds to a 30 degree differences in aAOS. Figure 3.5 shows an example of this phenomenon through the comparison of a shallower insertion and a deeper insertion for different patient STs for a fixed mAOS.
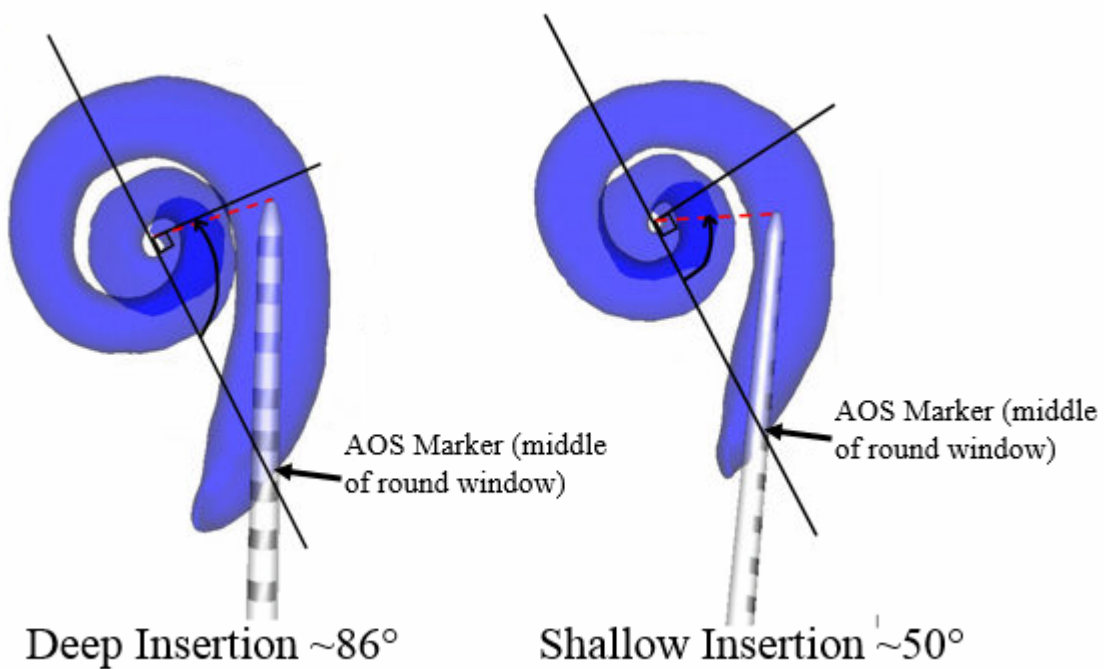
Figure 3.5: Comparison of a shallower insertion and a deeper insertion for different patient STs for a fixed mAOS.

The insertion simulation results are shown in Figure 3.6 and 3.7. In the figure, plots of mean and maximum distance across all subjects in our dataset between the simulated shape of the electrode array as it is advanced off the stylet into the cochlea and the optimal trajectory of the electrode array in the ST are shown. The x-axis corresponds to the amount
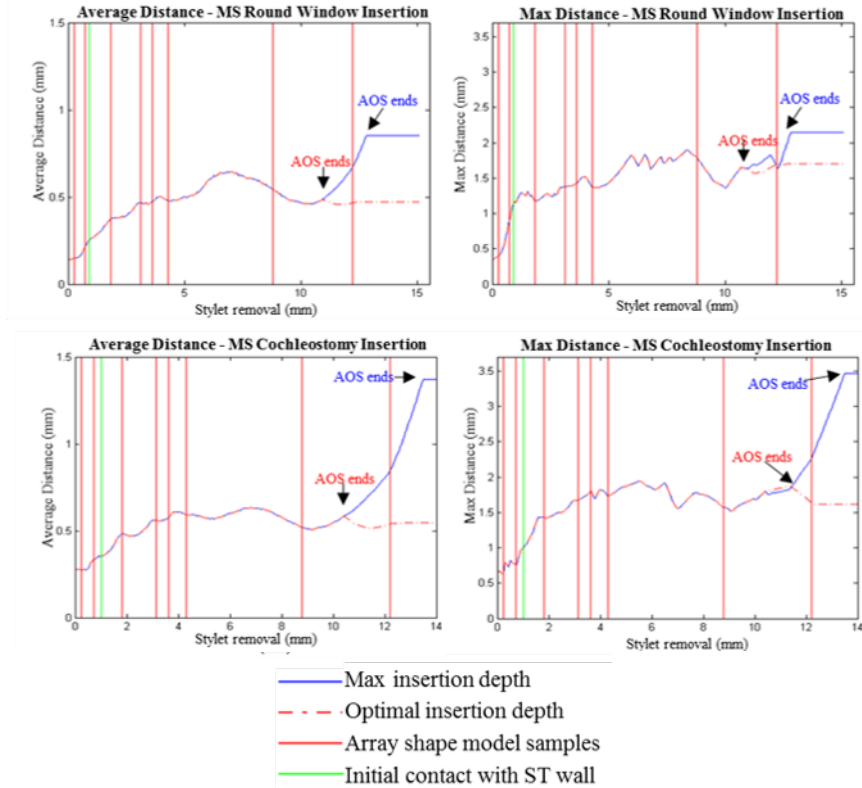
Figure 3.6: Plots of mean and maximum distance across all subjects in our dataset between the resting-state shape of the MS electrode array from our model and the midline of the scala tympani as the model electrode array; and CA electrode array from our model and the perimodiolar line of the scalatympani as the model electrode array is advanced off the stylet into the cochlea in our simulation

of stylet removal. The y-axis corresponds to the distance between the simulated and optimal insertion trajectories. The red vertical lines in the figure represent locations where the shape of the electrode array is equal to a single electrode array exemplar measured in CT as shown in Figure 3.3. i.e., these are locations where interpolating between array shapes is not necessary. Between the red lines the shape of the electrode array is interpolated between electrode array exemplars. To the right of the right-most red line the shape of the electrode array is the same as that of the last exemplar because the stylet has been removed far enough that the shape of the electrode array no longer changes. The blue curve shows the distance between the simulated and optimal insertion trajectory when the simulated electrode array is advanced

33
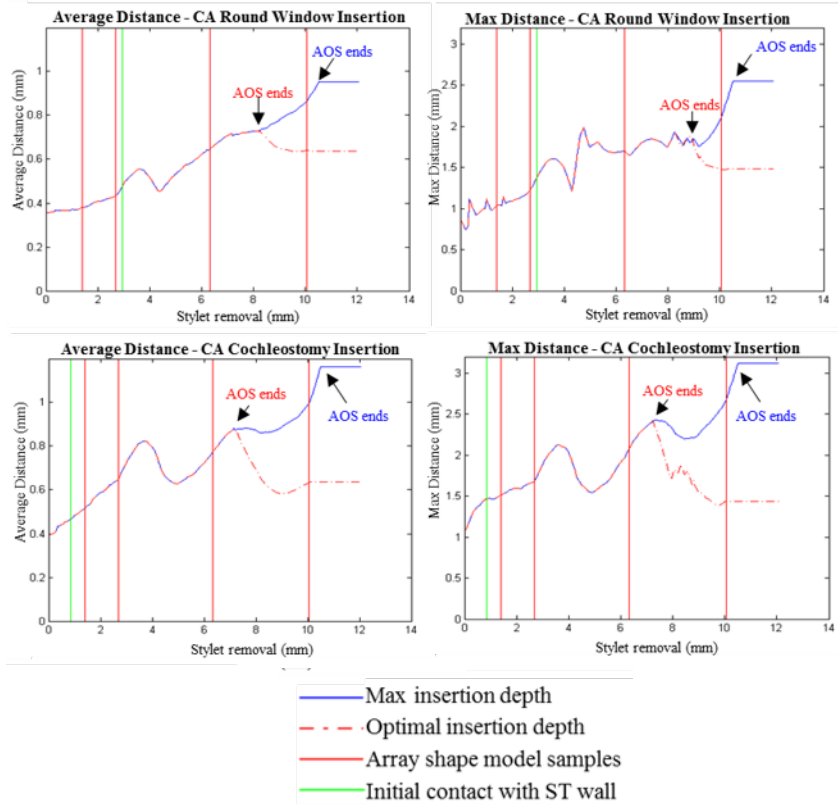
Figure 3.7: Plots of mean and maximum distance across all subjects in our dataset between the resting-state shape of the MS electrode array from our model and the midline of the scala tympani as the model electrode array; and CA electrode array from our model and the perimodiolar line of the scalatympani as the model electrode array is advanced off the stylet into the cochlea in our simulation

off the stylet until a maximum insertion depth is reached, i.e., the overall depth marker reaches the entry site (indicated by AOS ends in blue in the plots), and then the electrode array is no longer advanced and the stylet removed. As can be seen across all the sub-figures, the blue curves show there are relatively small distances between the simulated and optimal insertion trajectories for the first several millimeters of electrode array advancement, with mean distances between the simulated and optimal trajectories of around 0.5 mm. This indicates fair agreement between the simulated and optimal insertion trajectories. However, the blue curves all have relatively sharp increases on the right side of the plots, indicating substantial disagreement between the simulated and optimal insertion trajectories for the

34

last 2-3 mm of electrode array advancement. This increase in distance occurs because the last 2-3mm of electrode array advancement results in translating the electrode array model past the lateral wall of the first turn of the cochlea. This can be visualized in Figures 3.7a, c, e, and g on page 38. Translation of the electrode array model past the lateral wall of the cochlea is allowed in our simulation because we are only modeling the relaxed shape of the array in air without attempting to directly predict how the electrode array interacts with the walls of the ST. After observing the translation of the electrode array model past the lateral wall of the cochlea in these simulations, we re-ran our simulations while stopping the electrode array advancement procedure at an optimal depth. The optimal depth was determined by finding the average insertion depth across our dataset of STs that resulted in the best overall agreement with the optimal insertion trajectories. Our data show that the optimal depth corresponds to the depth at which the depth marker is approximately 2 mm outside the RW or CO entry site for the MS electrode arrays and the depth at which the middle marker rib is approximately 2 mm outside the entry site for the CA electrode arrays. In Figure 3.6, the red-dashed curve shows the distance between the simulated electrode array trajectory and the optimal insertion trajectory when the electrode array is advanced off the stylet until the simulated electrode array reaches the optimal depth (indicated by AOS ends in red in the plots), at which point the electrode array is no longer advanced and the stylet is fully removed. Figure 3.8b, d, f, and h show examples of the final position of the electrode arrays when inserting to the optimal depth in our simulations.

We additionally used our simulation technique to localize the off-stylet advancement distance in the insertion procedures at which the electrode array initially makes contact with the wall of the ST. The average advancement distance where this occurs is shown as the vertical green line in Figure 3.6 and representative cases are shown in 3D in Figure 3.8i-l. As can be seen Figure 3.8 the MS electrode arrays initially contact the modiolar wall of the ST whereas the CA electrode arrays initially contact the lateral wall.

35
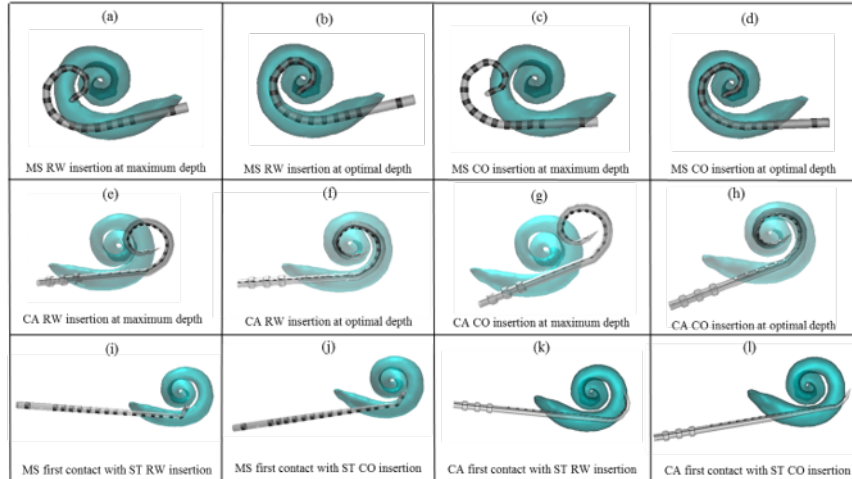
Figure 3.8: Final resting state shape of MS electrode array for a round window insertion placed at maximum depth (a) and optimal depth (b) and for a cochleostomy insertion at maximum depth (c) and optimal depth (d). Final resting state shape of CA electrode array for a round window insertion placed at maximum depth (e) and optimal depth (f) and for a cochleostomy insertion at maximum depth (g) and optimal depth (h). Position of MS (i,j) and CA (k,l) electrode arrays when they initially contact a wall of the ST

3.5 Conclusions

In this study, we have presented a novel approach for modeling the shape of pre-curved electrode arrays and a metric for evaluating the quality of an electrode insertion procedure with patient-specific ST geometry. When simulating electrode array placement, we chose to only model the resting-state shape of the electrode array in air without attempting to directly predict how the array interacts with the walls of the ST. We chose this approach because modeling the resting-state shape of the electrode array can be done reliably and accurately, while the accuracy of a method that attempts to predict the complicated behavior of the electrode array when interacting with the walls of individual cochleae is difficult if not impossible to validate. Although our approach is not a comprehensive physics-based model, our metric of insertion quality is able to characterize the distance between the relaxed shape of the electrode arrays and the shape of the ST, which indirectly characterizes the amount

of interaction with the walls of the ST that would be necessary to place the electrode array. We used this model and metric to evaluate insertion of CA and MS electrode arrays for STs of nine individuals. The results obtained from our models showed when electrodes are implanted at a maximal depth, which is the depth typically chosen by many surgeons, the resting state shape of the electrode arrays does not accurately match the shape of the ST. Rather, the last 2-3mm of electrode array advancement results in shifting the resting state of the electrode array past the lateral wall of the first turn of the cochlea. This indicates that during a real procedure, when inserting the electrode array to the maximum depth, the last 2-3 mm of advancement may not lead to further advancement of the tip of the electrode array but instead a lifting of the electrode array from the modiolar wall towards the lateral wall in the first turn of the cochlea. Non-perimodiolar placement of pre-curved electrode arrays has been linked to poorer outcomes [18] and could result in both (i) increased power consumption and poorer battery life and (ii) trauma to the basilar membrane in the first turn of the cochlea. To corroborate the hypothesis that maximum insertion depth could lead to a medial-to-lateral shift in the first turn, the placement of CA and MS electrode electrode arrays for several patients were identified using techniques we have previously proposed and validated for accurately localizing electrodes in patient CT images [29, 32, 33], and these electrode arrays were inspected to determine whether this phenomenon could be observed. Figure 3.9 shows electrode position for four individuals. Panels a and c are examples of the MS and CA electrode arrays inserted to a maximum depth. As can be seen the electrode arrays appear to be pushed against the lateral wall in the first turn of the cochlea. Panels b and d are examples that were inserted to a shallower depth. In these cases both electrode arrays maintain a perimodiolar positioning in the first turn of the cochlea. Thus, this data from real patients appears to corroborate what we predict from the results of our simulations.

These preliminary findings indicate that further investigation of optimized insertion depths with CA and MS electrode arrays is warranted, as optimizing depth may permit
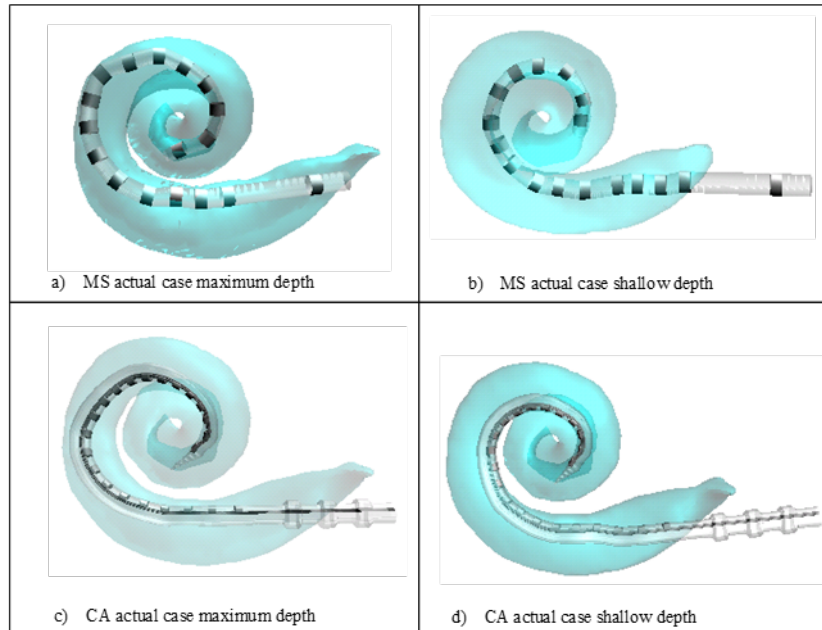
Figure 3.9: Electrode position for four CI recipients measured from CT scans showing deep (a and c) and shallow (b and d) implantations for both MS and CA

achieving modiolar-hugging electrode array positioning. The results we report are too preliminary to define a specific insertion depth that would be best. It is important to note there are potential negative side effects that could result from insertion depths that are too shallow, e.g., shallower insertion depth might result in shallower angular depth of distal contacts, which would reduce ability to activate lower frequency neural regions, and would certainly result in shallower angular depth of proximal contacts, which could result in more proximal contacts becoming unusable. Further studies are needed to weigh the positive effects of better modiolar positioning against such potential negative side effects. Other future investigations will include temporal bone studies to verify that an optimized insertion depth results in better modiolar placement of pre-curved electrode arrays.

The results in this section also indicate that there is substantial variability across individual cochleae in what is optimal with respect to the AOS depth, and relatively small differences of 1.5-2 mm in AOS depth leads to relatively large variations of up to 30 degrees

in angular AOS depth. Figure 3.5 illustrates this variability in cochleae by comparing a shallower aAOS to that of a deeper aAOS for two different patients fixed at the same mAOS. Angular AOS positions that are too deep can lead to translocation of the electrode array from the ST into the scala vestibuli, which is linked to poorer outcomes [5]. Angular AOS positions that are too shallow can cause the electrode array tip to be lodged in the basal turn of the cochlea and lead to folding of the electrode array, which is also highly detrimental to outcomes. This patient-specific variability in angular AOS position suggests that a system that would facilitate patient-specific planning and guidance of electrode insertion procedures may improve electrode placement and ultimately hearing outcomes.

CHAPTER 4

CONCLUSION

Two different image processing applications were presented in this thesis. The first presents a novel approach for automatically segmenting the mastoid region for acoustic neuroma surgery. The intent is that this automatic patient-specific segmentation will be utilized in an acoustic neuroma surgery robot (ANSR) in order to complete the initial bone drilling for the surgeon. This would greatly reduce surgery time which would directly benefit both the surgeon and thus the patient. It does this by minimizing the likelihood of mental mistakes made by the surgeon due to fatigue later in the surgery. It also would greatly reduce the amount of time the patient is under anesthesia. Lastly, it reduces preoperative measures needed as the surgeon will no longer need to manually delineate the drilling region. Overall, the development of this automatic segmentation can supply the ANSR with a clear, accurate, and precise drilling pathway to reach the IAC and remove the acoustic neuroma which will greatly improve and expedite acoustic neuroma surgery.

The second image processing technique presents a proof-of concept study to support the need for patient-specific insertion plans for cochlear implant surgery. It has been shown previously that electrode array insertion into the cochlea is variable and this variability can result in differing hearing outcomes for different patients. This study shows that it is possible that shallower insertions into the ST can result in better hearing outcomes. This study also

shows evidence that there is ST variability between patients. Therefore, the development of patient-specific insertion plans based on the patient's preoperative CT could provide a consistent way to achieve better hearing outcomes for cochlear implant surgery.

Although not directly related, both techniques focus on aspects of the ear and both have the potential to greatly improve the quality of life of the patient.

4.1 Future Work

The next step for the first section presented in this thesis is to fully integrate with the ANSR system. As the automatic resection planning system and the ANSR system were designed separately, some extra integration planning may be necessary. Once the two systems have been integrated, extensive cadaver testing must be completed to insure that the full system is safe and reliable. Further changes to the automatic resection planning system will be completed pending the outcome of the cadaver studies. Once these future steps are completed satisfactorily, the ANSR system would be ready to begin clinical studies.

For the second portion of this thesis, one potential next step would be to complete similar studies to those presented on a larger data set. This will help ensure that the results presented in this paper, on a small data set, are consistent with those of a larger study. Pending similar results from a larger study, the next step would be to conduct a similar study on cadavers with expert surgeons completing a cochlear implant surgery on the cadavers with the suggested insertion depths. The final step is to complete clinical trials in which patients are surveyed following their surgery as to the quality of their hearing post-surgery after predicted insertion depths are utilized.

REFERENCES

[1] J. Kline, *Handbook of Biomedical Engineering*, 1st ed. Academic Press, San Diego, 1988.

[2] Acoustic neuromas what you should know. UT Health Science Center, Department of Neurosurgery. Last accessed: October, 2015. [Online]. Available: http://neurosurgery.uthscsa.edu

[3] G. B. Wanna, J. H. Noble, T. R. McRackan, B. M. Dawant, M. S. Dietrich, L. D. Watkins, A. Rivas, T. A. Schuman, and R. F. Labadie, "Assessment of electrode placement and audiological outcome in bilateral cochlear implantation," *Otol Neurotol*, vol. 32, no. 3, pp. 428–432, April 2011.

[4] G. B. Wanna, J. H. Noble, M. L. Carlson, R. H. Gifford, M. S. Dietrich, D. S. Haynes, B. M. Dawant, and R. F. Labadie, "Impact of electrode design and surgical approach on scalar location and cochlear implant outcomes," *Laryngoscope*, vol. 124, no. 0 6, pp. S1–S7, November 2014.

[5] Acoustic neuroma vestibular schwannoma. Mayfield Clinic. Last accessed: 2015. [Online]. Available: http://www.mayfieldclinic.com/PE-Acoustic

[6] J. M. Propp, B. J. McCarthy, F. G. Davis, and S. Preston-Martin, "Descriptive epidemiology of vestibular schwannomas," *Neuro-oncology*, vol. 8, no. 1, pp. 1–11, January 2006.

[7] N. Dillon, L. B. Kratchman, M. S. Dietrich, R. F. Labadie, R. J. 3rd Webster, and T. J. Withrow, "An experimental evaluation of the force requirements for robotic mastoidectomy," *Otology and Neurotology*, vol. 34, no. 7, pp. 93–102, September 2013.

[8] N. Dillon, R. Balachandran, A. M. dit Falisse, G. B. Wanna, R. F. Labadie, T. J. Withrow, J. M. Fitzpatrick, and R. J. Webster, "Preliminary testing of a compact, bone-attached robot for otologic surgery," *Proceedings of SPIE-the International Society of Optical Engineering*, vol. 9036, no. 4, pp. 903 614–, March 2014.

[9] J. H. Noble, B. M. Dawant, F. M. Warren, and R. F. Labadie, "Automatic identification and 3d rendering of temporal bone anatomy," *Otology and Neurotology*, vol. 30, no. 4, pp. 436–442, June 2009.

[10] F. Reda, T. R. McRackan, R. F. Labadie, B. M. Dawant, and J. H. Noble, "Automatic segmentation of intra-cochlear anatomy in post-implantation ct of unilateral cochlear implant recipients," *Medical Image Analysis*, vol. 18, no. 3, pp. 605–615, April 2014.

[11] J. Noble, F. M. Warren, R. F. Labadie, and B. M. Dawant, "Automatic segmentation of the facial nerve and chorda tympani in ct images using spatially dependent feature values," *Medical Physics*, vol. 35, no. 12, pp. 5375–5384, December 2008.

[12] L. R. Dice, "Measures of the amount of ecologic association between species," *Ecology*, vol. 26, no. 3, pp. 297–302, July 1945.

[13] B. Tolsdorff, A. Petersik, B. Pflesser, A. Pommert, U. Tiede, R. Leuwer, and K. H. Hohne, "Individual models for virtual bone drilling in mastoid surgery," *Computer Aided Surgery*, vol. 14, no. 1-3, pp. 21–27, 2009.

[14] Cochlear implants. National Institute on Deafness and Other Communication Disorders (NIDCD). Last accessed: March 5, 2015. [Online]. Available: http://www.nidcd.nih.gov/health/hearing/pages/coch.aspx.

[15] G. J. Basura, O. F. Adunka, and C. A. Buchman, "Scala tympani cochleostomy for cochlear implantation," *Operative Techniques in Otolaryngology-Head and Neck Surgery*, vol. 21, no. 4, pp. 218–222, December 2010.

[16] J. T. Roland, "A model for cochlear implant electrode insertion and force evaluation: Results with a new electrode design and insertion technique," *Laryngoscope*, vol. 115, no. 8, pp. 1325–1339, August 2005.

[17] T. Rau, A. Hussong, M. Leinung, T. Lenarz, and O. Majdani, "Automated insertion of performed cochlear implant electrodes: evaluation of curling behaviour and insertion forces on an artificial cochlear model," *International Journal of Computer Assisted Radiology and Surgery*, vol. 5, no. 2, pp. 173–181, March 2010.

[18] L. K. Holden, C. C. Finley, J. B. Firszt, T. A. Holden, C. Brenner, L. G. Potts, B. D. Gotter, S. S. Vanderhoof, K. Mispagel, G. Heydebrand, and M. W. Skinner, "Factors affecting open-set word recognition in adults with cochlear implants," *Ear Hear*, vol. 34, no. 3, pp. 342–360, May 2013.

[19] C. C. Finley, T. A. Holden, L. K. Holden, B. R. Whiting, R. A. Chole, G. J. Neely, T. E. Hullar, and M. W. Skinner, "Role of electrode placement as a contributor to variability in cochlear implant outcomes," *Otol Neurotol*, vol. 29, no. 7, pp. 920–928, October 2008.

[20] M. F. Dorman, P. C. Loizou, and D. Rainey, "Simulating the effect of cochlear-implant electrode insertion depth on speech understanding," *The Journal of the Acoustical Society of America*, vol. 102, no. 5, pp. 2993–2996, November 1997.

[21] M. W. Skinner, P. L. Amdt, and S. J. Staller, "Nucleus 24 advanced encoder conversion study: performance versus preference," *Ear Hear*, vol. 23, no. 1, pp. 2S–17S, February 2002.

[22] K. Yukawa, L. Cohen, P. Blamey, B. Pyman, V. Tungvachirakul, and S. O'Leary, "Effects of insertion depth of cochlear implant electrodes upon speech perception," *Audiology and Neurotology*, vol. 9, no. 3, pp. 163–172, May 2004.

[23] J. H. Noble, R. H. Gifford, A. J. Hedley-Williams, B. M. Dawant, and R. F. Labadie, "Clinical evaluation of an image-guided cochlear implant programming strategy," *Audiology and Neurotology*, vol. 19, no. 6, pp. 400–411, November 2014.

[24] J. H. Noble, R. F. Labadie, R. H. Gifford, and B. M. Dawant, "Image-guidance enables new methods for customizing cochlear implant stimulation strategies," *IEEE Trans Neural Syst Rehabil Eng*, vol. 21, no. 5, pp. 820–829, September 2013.

[25] T. J. Balkany, A. A. Eshraghi, and N. Yang, "Modiolar proximity of three perimodiolar cochlear implant electrodes," *Acta Otolaryngol*, vol. 122, no. 4, pp. 363–369, June 2002.

[26] R. L. Turok, R. F. Labadie, G. B. Wanna, B. M. Dawant, and J. H. Noble, "Cochlear implant simulator for surgical technique analysis," *Proceedings of SPIE-the International Society of Optical Engineering*, vol. 9036, pp. 903 619–, 2014.

[27] H. Kha and B. Chen, "Finite element analysis of damage by cochlear implant electrode array's proximal section to the basilar membrane," *Otol Neurotol*, vol. 33, no. 7, pp. 1176–1180, September 2012.

[28] C. A. Todd and F. Naghdy, "Real-time modeling and simulation for cochlear implantation; visualization and force rendering during virtual prosthetic insertions," *International Journal of Modeling and Optimization*, vol. 2, no. 4, pp. 518–523, August 2012.

[29] J. H. Noble, R. F. Labadie, O. Majdani, and B. M. Dawant, "Automatic segmentation of intracochlear anatomy in conventional ct," *IEEE Trans Biomed Eng*, vol. 58, no. 9, pp. 2625–2632, September 2011.

[30] B. M. Verbist, M. W. skinner, L. T. Cohen, P. Leake, C. James, C. Boex, T. A. Holden, C. C. Finley, P. S. Roland, J. T. Roland, M. Haller, J. F. Patrick, C. N. Jolly, and M. A. Faltys, "Consensus panel on a cochlear coordinate system applicable in histological, physiological and radiological studies of the human cochlea," *Otol Neurotol*, vol. 31, no. 5, pp. 722–730, July 2010.

[31] S. Bouix, K. Siddiqi, and A. Tannenbaum, "Flux driven automatic centerline extraction," *Med Image Anal*, vol. 9, no. 3, pp. 209–221, June 2005.

[32] T. A. Schuman, J. H. Noble, C. G. Wright, G. B. Wanna, B. Dawant, and R. F. Labadie, "Anatomic verification of a novel, non-rigid registration method for precise

intrascalar localization of cochlear implant electrodes in adult human temporal bones using clinically-available computerized tomography," *Laryngoscope*, vol. 120, no. 11, pp. 2277–2283, November 2010.

[33] Y. Zhao, B. M. Dawant, R. F. Labadie, and J. H. Noble, "Automatic localization of cochlear implant electrodes in ct," *Med Image Comput Comput Assist Interv*, vol. 17, no. 1, pp. 331–338, May 2015.